



Flow rate improvements in additively manufactured flow channels suitable for rocket engine application

Maximilian Buchholz¹ · Samira Gruber³ · Alex Selbmann³ · Axel Marquardt^{2,3} · Lucas Meier² · Michael Müller^{2,3} · Lukas Seifert¹ · Christoph Leyens^{2,3} · Martin Tajmar¹ · Christian Bach¹

Received: 31 March 2022 / Revised: 1 September 2022 / Accepted: 7 October 2022 / Published online: 27 October 2022
© The Author(s) 2022

Abstract

This contribution describes the investigation of flow channels which are designed to be directly integrated into an aerospike engine by means of additive manufacturing with laser powder bed fusion (LPBF). During the experimental testing of a previous aerospike engine in 2019, it was observed that high surface roughness of such additively manufactured integrated channels caused a significant reduction in the mass flow rates of the propellants ethanol and liquid oxygen as well as the coolant due to increased pressure drop. In an extensive study within the CFDMikroSAT project, various factors influencing this surface roughness are, therefore, being investigated, which include the geometry of the channels as well as selected manufacturing parameters of the LPBF process, such as layer thickness and component orientation. To further reduce the roughness after manufacturing, suitable post-processing methods are also being investigated for internal cavities, initially analysing the abrasive flow machining process. Within the paper, the overall investigation approach is presented, such as the overview of the considered specimens, and the initial results of a various studies with selected specimens are discussed. These studies consist of the examination of surface roughness reduction, shape accuracy and flow behaviour of post-processed cooling channel specimens. Finally, a brief overview of the already manufactured aerospike demonstrator is presented.

Keywords Additive manufacturing · Abrasive flow machining · Aerospace components · Aerospike engine · Flow channels · Laser powder bed fusion

Abbreviations

AFM	Abrasive flow machining
IfWW	Institute of Material Science
ILR	Institute of Aerospace Engineering
IWS	Fraunhofer Institute for Material and Beam Technology
LPBF	Laser powder bed fusion
NASA	National Aeronautics and Space Administration
PH	Precipitation hardened
SA	Solution annealed
TUD	Technische Universität Dresden

1 Introduction

Advanced materials and innovative manufacturing techniques are important technology drivers for the future development of propulsion systems in the aerospace industry. The use of additive manufacturing processes in combination with so-called superalloys currently offers such development potential [1, 2]. Additive manufacturing, often also referred to as 3D printing, is a collective term for a group of manufacturing methods that are characterised in particular by their layer-by-layer production of components [3].

A comprehensive report, published in 2018 by the US National Aeronautics and Space Administration (NASA), describes a wide range of applications for additive manufacturing that are suitable for space technology and especially for engine development. For example, the advantages of these manufacturing methods can be used for one-piece designs of injectors or ignition mechanisms, or to produce combustion chambers and nozzles with integrated cooling circuits [4].

✉ Maximilian Buchholz
maximilian.buchholz@tu-dresden.de

¹ Institute of Aerospace Engineering, TU Dresden, 01062 Dresden, Germany

² Institute of Materials Science, TU Dresden, 01062 Dresden, Germany

³ Fraunhofer Institute for Material and Beam Technology, 01277 Dresden, Germany

While the investigations presented in this report primarily focused on conventional engine designs with bell nozzles, the use of additive manufacturing methods also offers advantages for alternative designs. One such design is the aerospike engine, which is currently a research focus at the Institute of Aerospace Engineering (ILR) of the Technische Universität Dresden (TUD). This particular type of engine is characterised by its potential to adapt to the varying ambient pressure as it passes through the atmosphere. This characteristic is achieved by the aerospike nozzle (alternatively also called plug nozzle), which, unlike classic Laval nozzles, does not have a fixed, outer boundary to its expansion range. Instead, the exiting exhaust flow is contained by the surrounding free jet and limited on the inside by the spike that gives the nozzle its name (see Fig. 1) [5].

While the altitude-adaptive properties of aerospike engines show great potential for improving the performance of launchers, their design also presents a substantial technical challenge. The central body (spike) is located in the middle of the emerging hot gas and is, therefore, exposed to extremely high thermal loads during its entire operation. This circumstance necessitates the use of active cooling mechanisms, such as regenerative cooling, within the structure. Together with the relatively complex geometry of the central body, this results in significant difficulties in the conventional production of aerospike engines, which can be seen as one of the central reasons for their limited application to date [7].

A promising way to reduce these challenges can be found in the use of the additive manufacturing processes mentioned above. The layered structure of these manufacturing processes enables the direct implementation of internal channels into the spike, necessary for cooling, while at

the same time creating the flow-relevant, external contour. Although this manufacturing method offers great potential for aerospike engines, the use of additive manufacturing processes also presents various challenges. Foremost is the relatively high surface roughness of additively manufactured components, which can have a detrimental effect on the flow behaviour of fluids.

In this article, this challenge is discussed and possible strategies for improving the surface quality of additively manufactured engine components are presented. The investigation of this topic is subject of the CFDMikroSAT cooperation project, carried out by the ILR, the Fraunhofer Institute for Material and Beam Technology (IWS) and the Institute for Material Science (IfWW) of the TUD. While it is assumed that a certain roughness of flow channels can have a positive effect on the heat transfer to coolants, the investigations presented initially focus exclusively on a reduction of the pressure loss. A better understanding of how to generate a desired surface roughness by adjusting the manufacturing parameters and using selected post-processing methods will provide the foundation for later investigations to set targeted roughness parameters to generate an optimum of pressure drop and heat transfer.

In Sect. 2, additively manufactured aerospike engines are presented, which have been investigated within previous projects. Section 3 describes the methodology of the CFDMikroSAT project, including the manufacturing process used, the material selection and the experimental investigation approach. Section 4 presents the first results of a manufacturing study by the IWS and IfWW and Sect. 5 describes a study to improve the surface quality using the post-processing method abrasive flow machining (AFM) and the impact on the shape accuracy. In Sect. 6, a comprehensive analysis of the flow behaviour is presented, in which test specimens without and with post-processing via AFM were investigated. Finally, Sect. 7 briefly discusses the planned revision of an additively manufactured aerospike engine and demonstrates how the findings from the previous chapters are taken into account for this design.

2 Preliminary research

To investigate the potential of additive manufacturing for aerospike engines, several research projects have already been carried out by the ILR in collaboration with the Fraunhofer IWS. The initial approach was the development of an aerospike engine to demonstrate the potential of additive manufacturing using laser powder bed fusion (LPBF). The aerospike engine manufactured within this study was based on the design of a 30 kN engine scaled by $2/3$, which in addition had several internal features. This included integrated cooling channels in the combustion chamber wall and the

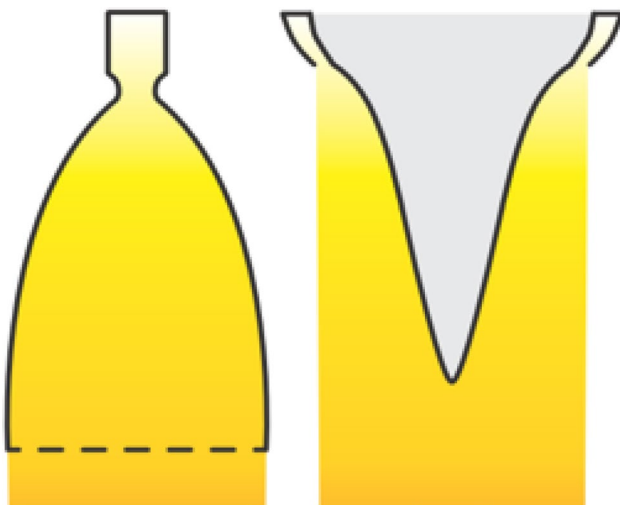


Fig. 1 Optimal expansion of the thrust jet for bell nozzle (left) and aerospike nozzle (right) [6]

spike, as well as additional ducts for fluid injection at the tip of the spike. To make the complex internal structures visible, a sectional model was created as part of the project, which can be seen in Fig. 2 [5].

This project was followed in 2019 by the development of an operational aerospike demonstrator. Designed for a nominal thrust of 500 N and a chamber pressure of 15 bar, this aerospike engine was designed by the ILR and manufactured by the Fraunhofer IWS using LPBF and subsequent mechanical post-processing. The thrust of 500 N was selected to allow experimental measurement of the engine at the existing facilities at ILR. The downscaling of an actively cooled aerospike engine creates some challenges here, as the temperature inside the combustion chamber drops only slightly with a much smaller surface area, resulting in a larger heat transfer. In addition, the smaller cooling channels also make additive manufacturing using LBPF more challenging. Conversely, verification of such an engine would allow the results to be transferred to a wider range of engines with higher thrust and larger dimensions.

In a following hot fire test campaign, the basic functionality of the engine was demonstrated by two successful burn tests using the fuel combination ethanol and liquid oxygen (see Fig. 3). However, during this test campaign, the measured performance parameters of the engine showed a significant deviation from the design parameters. These



Fig. 2 Additively manufactured cutaway model of the manufacturing demonstrator [5]



Fig. 3 Hot fire test of the 500 N aerospike engine

reduced performance parameters were primarily attributed to a limited mass flow rate of the injector due to increased pressure losses. Besides insufficient machining of the injector orifices, these additional pressure losses were primarily explained by high surface roughness within the propellant supply lines. A similar behaviour was observed in the integrated cooling channels of the spike and the combustion chamber wall, whereby high roughness values again induced additional pressure losses [8].

Therefore, there is a need for additional research of the surface quality of additively manufactured engine components. Here, it is important to determine the initial roughness as a function of the manufacturing parameters, as well as methods for further reducing the roughness values after manufacturing.

3 Methodology

To systematically investigate the multitude of interlinked aspects in the additive manufacturing of engine components, it is essential to analyse the entire process chain of this procedure. This includes the influence of various process parameters during manufacturing as well as the suitability and results of potential post-processing steps. Since the parameters investigated are dependent on the dimensions of the engine components, the initial approach is based on earlier engine designs of the ILR in the low to medium thrust category.

3.1 Flow channel specimens

An important first step in analysing the connection between additive manufacturing and achievable surface quality is the definition of the geometric boundary conditions to be investigated. To this end, the studies presented in this paper

initially focus on the boundary conditions of low to medium thrust engines. Using the findings, however, more general statements on the additive manufacturing of engine components for a wide range of application scenarios are also aimed for.

To determine the geometries, the design of the aerospike demonstrator from 2019 described above serves as a starting point, which can be further subdivided into the two areas of injector and cooling channels. Based on this subdivision, sub-segments with simple channel geometries can be determined to separately investigate the interaction between manufacturing and post-processing of specific geometries. Individual test specimens were designed for these sub-segments, which are derived from a matrix of channel cross-sections and shapes.

For the cross-sectional areas, circular geometries were selected to represent supply lines and manifolds of injectors. Rectangular cross-sections, on the other hand, represent channel geometries as found in cooling systems of the combustion chamber wall and the spike. The upper and lower dimensions of these cross-sectional areas were based on the conditions within the previous demonstrator. In addition, it was ensured that all cross-sectional areas could be manufactured without the use of support structures. Such support structures should generally be avoided for flow channels, as they have a considerable influence on the flow characteristics and the resulting pressure loss and are difficult to remove from internal cavities [9]. Table 1 shows the dimensions of the derived circular and rectangular cross-section geometries.

Similar to the cross-sectional geometries of the test specimens, their channel shapes are also designed to be as simple as possible, whereby the aim was again to represent the widest possible spectrum of courses in injectors or cooling systems of small engines such as the previously described aerospike engine. For each cross-section, there is initially a test specimen with a straight channel, which serves as a reference for the analyses. Further channel shapes represent geometric changes within the associated aerospike engine, which affect the induced pressure losses and changes in the

flow velocities of the traversing fluids. For instance, changes of 45° or 90° in the flow course represent conditions such as those found at the inlets or outlets of distributor rings for propellants or coolants. The transition from such distributor rings to individual rectangular cooling channels is again represented by the change in shape from circular to rectangular. The expansion or contraction of channels as well as segmentation represent areas where the flow velocity has to be adjusted due to peaks in local heat transfer.

The pressure loss and velocity changes resulting from the described channels are of interest both for the flow of cooling fluids and propellants as well as for post-processing techniques based on abrasive fluids. One such process is abrasive flow machining (AFM), which is described in more detail in Sect. 3.4. The following overview summarises all channel shapes which, in combination with the cross-sections presented in Table 1, form the resulting test specimens. Examples of these specimens can be seen in the sectional views of the CAD models in Fig. 4.

Geometries utilized as channel shapes:

- Straight channel with 100 mm length (reference)
- Change of flow direction for $2 \times 45^\circ$ (a) and $2 \times 90^\circ$
- Segmentation into two individual channels (b)
- Change in cross-section from circular to rectangular (c)
- Reduction of the channel cross-section by 50% (d)

The combination of the described, different cross-sectional geometries and channel courses results in 34 different test specimens. Some combinations have already been excluded, such as halving the cross-sectional area of circular specimens with a diameter of 2 mm or rectangular ones with

Table 1 Cross-sectional dimensions of the flow channel specimens

Rectangular height \times width in mm
2 \times 1
4 \times 1
4 \times 2
8 \times 1
8 \times 2
Circular diameter in mm
2
4
8

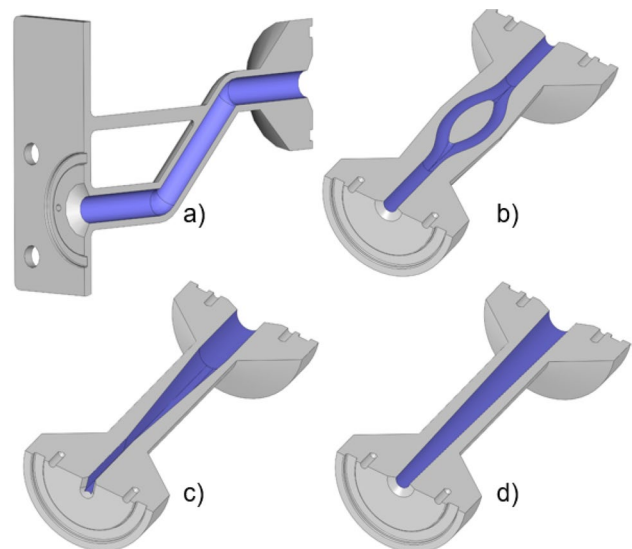


Fig. 4 Sectional view of selected flow channel specimens (flow-relevant surfaces indicated in blue)

a channel width of 1 mm. All successfully manufactured and investigated specimens are presented in Sect. 6 together with the results of the flow tests.

3.2 Manufacturing process

The LPBF manufacturing process was selected because it has a significantly higher resolution than other powder-based manufacturing methods, which in turn is crucial for ensuring a good surface quality [10].

To manufacture components using LPBF, a very thin layer of powder in the range of 20–100 μm is first applied to a building platform. This powder bed is then melted along a previously defined contour using a laser beam, whereby the path of the laser is realised by the deflection on an adjustable mirror. After the resulting molten bath has cured, the building platform is lowered by a defined layer thickness and the previously described process repeats. The penetration depth of the laser beam is selected in such a way that the newly applied powder layer is bonded to the already cured layer underneath. The combination of hundreds to thousands of individual layers produces the desired component. The entire LPBF process takes place in an inert gas atmosphere, which prevents both the oxidation of the finished layers and the ignition of fine powder particles [11]. A schematic overview of the process can be seen in Fig. 5.

3.3 Material selection

The nickel-based alloy INCONEL[®] 718 was chosen as the material for manufacturing the test specimens presented in Sect. 3.1. Alongside the titanium alloy Ti-6Al-4V, this material is frequently used in aerospace engines and is considered also for other high-temperature space applications. While titanium alloys offer lightweight advantages over INCONEL[®] 718 in a direct comparison, they are also generally associated with higher material costs. In addition, INCONEL[®] 718 has higher operating temperatures without compromising mechanical properties (600–650 $^{\circ}\text{C}$),

generally higher values for strength and elongation at break, and almost twice the Young's modulus [13–15]. One fundamental commonality of these materials, however, is the difficult mechanical post-processing with conventional tools due to their high hardness, which leads to increased tool wear [16]. In addition to the reasons of practicability already mentioned, post-processing with the non-tool-based abrasive flow grinding method presented in Sect. 3.4 thus represents an interesting technique for both materials.

INCONEL[®] 718 has very good mechanical properties at an operating temperature of up to 700 $^{\circ}\text{C}$, which is essential, considering gas temperatures of up to 2400 K in the combustion chamber of aerospike engines. Although this means that active cooling mechanisms are still necessary, the amount of heat to be dissipated by the cooling system can be reduced by such a high operating temperature [17].

A disadvantage is the thermal conductivity of INCONEL[®] 718, which is only about 24.1 W/mK at 700 $^{\circ}\text{C}$. This low thermal conductivity poses the risk that the heat absorbed by the material cannot be transferred sufficiently quickly into the cooling fluid. This might result in a potential risk to the structural integrity of the combustion chamber and the spike of an aerospike engine, despite the high operating temperature of INCONEL[®] 718. To counteract this potential risk, it is important to keep the wall thickness of the cooled engine components at a minimum to achieve the best possible heat transfer between the material and the cooling fluid [17].

Another significant characteristic of INCONEL[®] 718 is its high corrosion resistance. This corrosion resistance is crucial when using liquid oxygen, which has been pointed out in previous combustion tests of aerospike engines. Hereby, the hot work tool steel X40CrMoV5-1 was used for the demonstrator presented in Sect. 2. While this material has comparable mechanical properties to INCONEL[®] 718, the corrosion resistance is lower. In the subsequent test campaign, strong oxidation of the combustion chamber and the spike was observed, that can be seen in Fig. 6 [8, 17, 18].

3.4 Post-processing methods

Post-processing methods play a decisive role in improving the surface quality of flow-relevant areas. To achieve the desired surface quality for exposed surfaces, such as the inner wall of the combustion chamber and the outer side of the spike, a variety of conventional processes, such as turning or milling, are suitable. Difficulties for such processes, however, arise from the integration of internal cavities, for instance when using an integrated cooling system. These channels, some of which are quite small and intertwined, are not accessible using the aforementioned methods, although, particularly at this point, increased roughness values have a significant influence on the pressure loss that occurs.

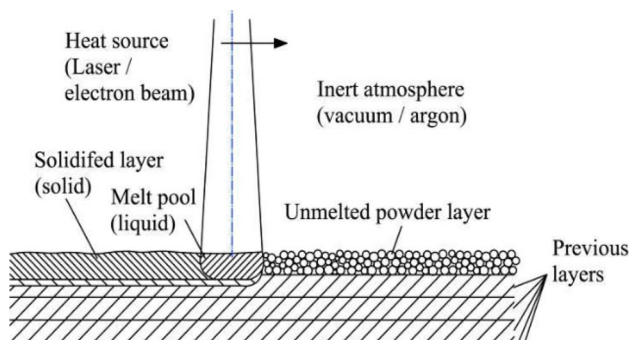


Fig. 5 Working principle of the LPBF process [12]



Fig. 6 Corrosion on the outside of the 2019 aerospike demonstrator made of X40CrMoV5-1

Within the presented investigations, the post-processing method of abrasive flow machining (AFM) was initially used. AFM is a grinding process in which the material removal is caused by the interaction between the solid material and an abrasive fluid. This abrasive fluid consists of a highly viscous carrier medium and added particles of very high hardness. For these particles, materials such as boron or silicon carbide are used. The channels or cavities to be reworked are filled with these fluids and are then pressurized to very high pressure in the range of up to 150 bar. The pressure can be generated either in one direction only or alternating between two pistons, whereby the latter can also be achieved indirectly by rotating the component after a certain processing time [19, 20] (Fig. 7).

The surface quality and material removal rate can be adjusted by the extrusion pressure of the pistons, the processing time, the temperature and the choice of fluid. For the abrasive fluid, the viscosity of the carrier medium and the properties of the particles used, such as their hardness, grain size or concentration, can be adjusted [22].

3.5 Experimental flow studies

To determine the influence of the surface roughness on the induced pressure drop, flow analyses of the test specimens presented in Sect. 3.1 are an appropriate method. The aim of these flow analyses is to determine the ratio of volume flow Q and pressure loss Δp for the flow through the test specimens. Subsequently, with a known density ρ , the kV value can be calculated, with its unit given in m^3/h or l/s :

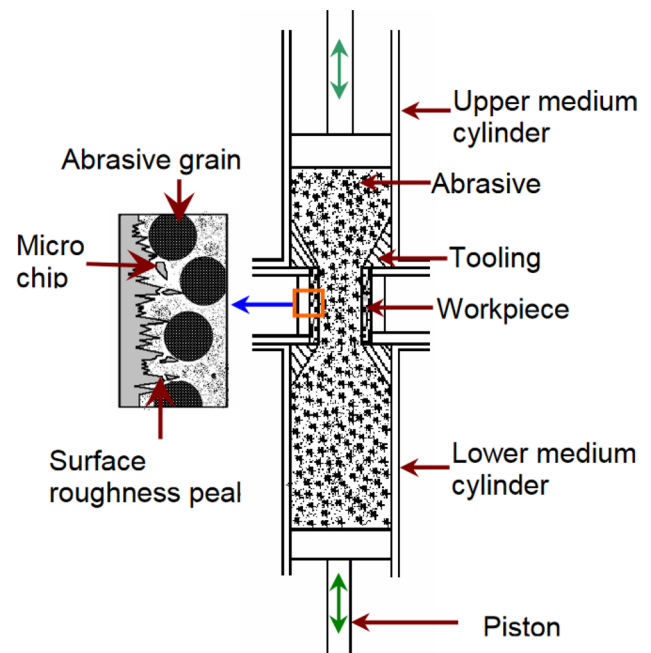


Fig. 7 Layout and working principle of the two-way AFM process [21]

$$kV = Q \times \sqrt{\frac{1\text{bar}}{\Delta p} \times \frac{\rho}{1000 \frac{\text{kg}}{\text{m}^3}}}. \quad (1)$$

This parameter is used in the characterisation of hydraulic components and provides a consistent reference value for the pressure loss, even at variable flow rates. With the help of this reference value, conclusions can be made about the influence of the AFM process on the pressure loss characteristics of different geometries by measuring the test specimens presented in Sect. 3.1. Thus, the increase in the kV value can be used to derive a measure of the reduction in pressure loss due to specific post-processing steps.

While these flow analyses are initially only carried out for individual segments of channels in the form of the aforementioned test specimens (results discussed in Sect. 6), it is also of interest to apply this procedure to the post-processing of the entire cooling system in the further development.

4 Manufacturing studies

A decisive first step in the definition of a process chain is the consideration of the operating conditions of the desired components and the material requirements derived from them. In the additive manufacturing of engine components, on the one hand, the mechanical resilience to the high combustion chamber pressure and occurring pressure spikes during ignition are important. Furthermore, heat conduction through

the material is also crucial for the active cooling of these components to ensure the removal of high heat loads during combustion tests.

At the beginning of the CFDMikroSAT project, manufacturing studies were carried out, in which both the influence of the layer thickness and the overhang angle on the resulting material properties were investigated. The following sections describe the used approach as well as some selected results of these manufacturing studies.

4.1 Defect volume

A significant influence on the material properties has the selection of a suitable layer thickness during the manufacturing process. The layer thickness is an essential process parameter for the LPBF method, whose increase reduces the manufacturing time, but at the same time can result in a deterioration of the mechanical properties of the manufactured components. These reduced mechanical properties result from the increased energy required to bond larger layer thicknesses together, which can be achieved either by increasing laser power or by reducing scan speed or hatch distance. In turn, this can lead to local overheating of the material, which increases the probability of defects occurring for larger layer thicknesses.

In addition to the reduced mechanical properties, a large defect volume also reduces the effective heat transfer through the material. This effect results from the lower thermal conductivity of the inert gases, which are trapped in the resulting cavities during the manufacturing process.

To investigate the defect volume, the Fraunhofer IWS fabricated density cubes whose porosity was subsequently analysed using image processing software on metallographic microsections. The number of occurring defects, their size and the total porosity were determined. The selected layer thicknesses were 30 and 60 μm . This selection was made as a compromise between the INCONEL[®] 718 powder size between 15 and 45 μm and the laser beam diameter of 70 μm . Larger layer thicknesses are not feasible due to the maximum laser power of 200 W and the given laser beam diameter.

Figure 8 shows microsections of the tensile samples discussed below, since the differences in occurring defects are more clearly visible compared to the images of the density cubes due to the given resolution. It can be illustrated that the sample on the right with a layer thickness of 60 μm has significantly higher number of bonding defects. At the same time, the resulting voids are considerably larger compared to the sample with a layer thickness of 30 μm shown on the left. The image processing results showed a total porosity of about 3% for 30 μm layer thickness and up to 14% for 60 μm for the aforementioned density cubes.

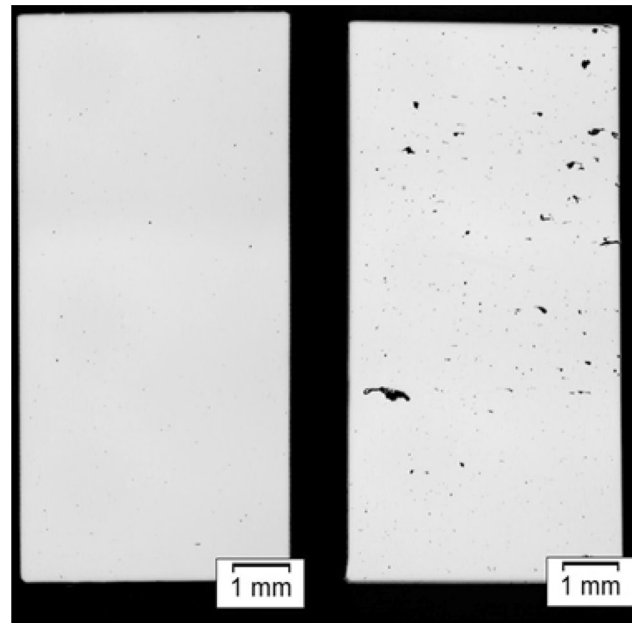


Fig. 8 Light microscope images of cuts through tensile specimen with a layer thickness of 30 μm (left) and 60 μm (right)

Additional tensile tests with samples of both layer thicknesses further verified the correlation between defect volume and reduced mechanical properties. Thus, tensile test samples with 30 μm layer thickness showed up to 12.8% higher tensile strength as well as an almost tripled elongation at break in the horizontal direction. Furthermore, it can be assumed that for cyclic loads the influence of the inclusions on the fatigue strength is more pronounced than in these static tensile tests. For such cyclic loads, the enclosed defects pose a great risk as crack initiation points. Based on these findings and the aforementioned improved thermal conductivity of lower layer thicknesses, a manufacturing with a layer thickness of 30 μm was defined for the further investigations.

4.2 Effect of overhang angles

A major factor influencing the surface roughness during additive manufacturing is the overhang angle. It describes the angle α between the horizontal build platform to the components build on it (see Fig. 9).

Figure 9 also shows that when determining the roughness induced by the overhang angle, a distinction must be made between the top side (“up-skin”) and the bottom side (“down-skin”).

While the previously presented layer thickness also has an influence on this resulting surface roughness, the results described below will initially focus on the analysis of samples with 30 μm layer thickness. In general, however, it can be said that a lower layer thickness also lowers the roughness

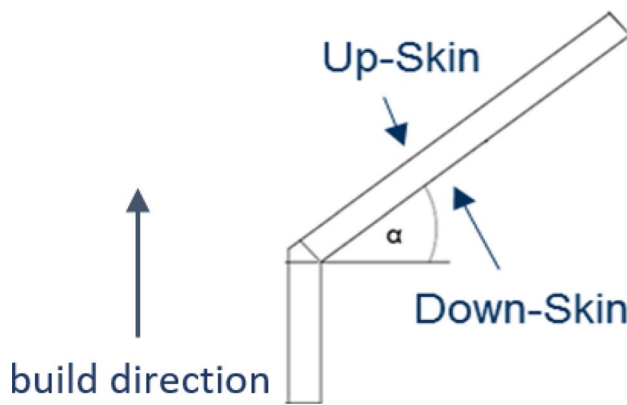


Fig. 9 Definition of the overhang angle α and the up- and down-skin areas

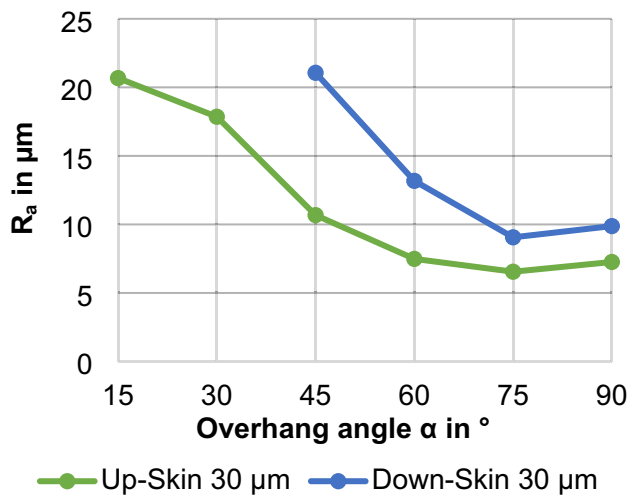


Fig. 10 Mean roughness R_a depending on the overhang angle α for samples with a layer thickness of $30\ \mu\text{m}$

values, as the influence of the so-called “staircase effect” is reduced [23]. Therefore, the roughness values for a $60\ \mu\text{m}$ layer thickness were in principle higher for all investigated overhang angles.

Figure 10 clearly shows that the mean roughness R_a generally increases as α is reduced, with a clear increase between 60° and 30° . Over the entire measuring range, higher roughness values are observed on the bottom side of the samples. It is also evident that no determination of the roughness values on the bottom side of the specimens was carried out for angles smaller than 45° , as support structures on the bottom side of the specimens are necessary to build up such overhangs. The increases in up-skin and down-skin roughness at 90° are marginal and can be attributed to measurement inaccuracies as well as the spread of the averaged roughness values.

For the design of additively manufactured components, these results imply that low overhang angles for flow-relevant surfaces should be avoided, if possible, especially at positions that might prove complicated to post-process. As the design conditions of the desired engine components do not allow this in every case, a carefully considered orientation on the building platform and the use of the post-processing methods discussed below are of great importance for low roughness results.

5 Abrasive flow machining studies

Apart from the possibilities to reduce the initial surface roughness of additively manufactured components, which are described in Sect. 4, this chapter will discuss first results associated with the AFM post-processing method described in Sect. 3.4.

The specimens considered in this preliminary study comprised only straight channels with a length of $50\ \text{mm}$, whose cross-sectional areas correspond to the maximum and minimum dimensions of the circular and rectangular geometries in Table 1. Therefore, the cross-sections examined measured $2\ \text{mm}$ and $8\ \text{mm}$ in diameter for circular specimens whereas $2 \times 1\ \text{mm}^2$ and $8 \times 2\ \text{mm}^2$ were selected for rectangular specimens. These four specimens were manufactured three times in one build job to investigate the influence of different heat treatment procedures on the results of the AFM process. For this purpose, all specimens were first solution annealed at $950\ ^\circ\text{C}$ for $2\ \text{h}$ in an argon atmosphere to reduce internal stresses within the components. Half of the specimens were then additionally heat treated according to AMS5662 at $720\ ^\circ\text{C}$ and $620\ ^\circ\text{C}$ for $8\ \text{h}$ in an argon atmosphere with the aim of precipitation hardening representing the ready-to-use state. In summary, for each cross-section variant there were two samples in the solution-annealed state and one sample in the precipitation-hardened state, resulting in a total number of samples examined in the preliminary AFM study of twelve.

For the post-processing by means of AFM, the Vector 200 system by ExtrudeHone was used, whereby the post-processing was carried out at the industrial partner AM Metals. Using this system, all samples were post-processed by one-way AFM, although the processing direction was inverted roughly halfway through the process. It was refrained from directly using a closed two-way process, since the observation of the emerging abrasive fluid provided information about the current processing state. This approach resulted in all test specimens being processed without counterpressure. Standard medium from ExtrudeHone were initially investigated as abrasive media for the post-processing. An iterative approach was used, in which the grain size of the media used was reduced depending on the achievable flow

rate during AFM. For all ExtrudeHone media, the abrasive fluid consisted of a carrier fluid of polyborosiloxane polymers with silicon carbide particles. The particle sizes used were 710 μm , 328 μm and 66 μm . Generally, however, it was observed that particle sizes of 710 μm were only applicable for circular channels with a diameter of 8 mm. For the channels with the smallest cross-sectional area of $2 \times 1 \text{ mm}^2$, post-processing could only be achieved with a particle size of 66 μm , albeit with the formation of cavitation-like spalling, which is described in Sect. 5.1. For the post-processing of the third set of samples, which was only solution annealed, the abrasive media was changed to media of the company 4MI, whose composition is subject to confidentiality. The results were comparable to those obtained with the ExtrudeHone media, using similar extrusion pressures between 30 and 40 bar. Processing temperatures were slightly lower for 4MI media, at about 20 °C, than those of ExtrudeHone, ranging from about 25–40 °C. Reasonable statements regarding the processing time and the total amount of abrasive medium used per specimen cannot be made due to the multiple media changes for each specimen.

Below, the correlation between heat treatment and post-processing is discussed, which is of particular importance in the previously mentioned generation of a comprehensive process chain for the additive manufacturing of engine components. For this purpose, both the achievable reduction in surface roughness and the shape accuracy are addressed.

5.1 Surface roughness reduction

To determine the initial surface roughness of the samples, negative silicone imprints of the channels were made, which were subsequently measured by optical means using a Keyence VR-3000 wide area 3D measurement system". According to the involved industry partner AM Metals, this method has already been verified in the past against optical methods with a Keyence VK-X250 confocal laser scanning microscope as well as tactile measurements and showed deviations of Rz of only about 1 μm . After the AFM process had been carried out, this procedure was repeated and the roughness values determined were compared.

Table 2 shows the results of the optical roughness measurement of the negative imprints. Depicted are the mean roughness values R_a for the two larger cross-section geometries as well as the comparison between the solution annealed and the precipitation-hardened condition.

The average values shown in Table 2 indicate that a significant reduction in the mean roughness R_a can be generally achieved with the help of the AFM process. A reduction of R_a between 92.3% and 95.1% was shown for the post-processing of samples with large cross-sectional geometries ($\varnothing 8 \text{ mm}$). On the other hand, however, the results do not yet provide clear statements on the influence of the heat

Table 2 Mean roughness R_a before (BP) and after (AP) post-processing with AFM and depending on the heat treatment used

	Solution annealed		Precipitation hardened	
	R_a BP	R_a AP	R_a BP	R_a AP
$\varnothing 8 \text{ mm}$	4.11 μm	0.20 μm	4.65 μm	0.23 μm
$8 \times 2 \text{ mm}^2$	4.94 μm	0.38 μm	4.05 μm	0.26 μm
R_a reduction				
$\varnothing 8 \text{ mm}$	95.1%		95.1%	
$8 \times 2 \text{ mm}^2$	92.3%		93.6%	

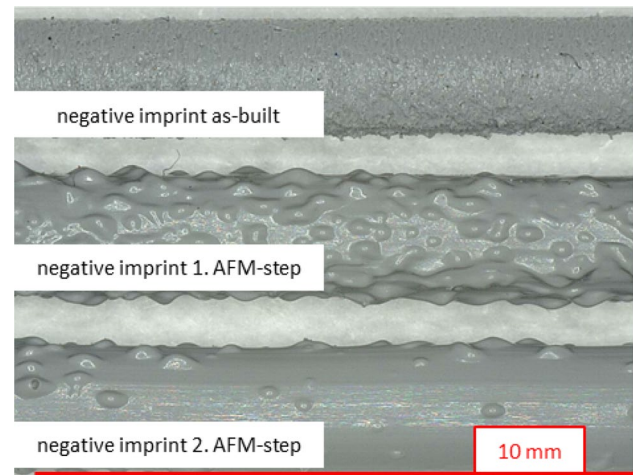


Fig. 11 Negative imprints of a channel with a diameter of 2 mm before post-processing (top), after 1st (middle) and 2nd (bottom) post-processing step using AFM

treatment. Based on the values determined, the achievable reduction in surface roughness appears to be predominantly dependent on the initial roughness after manufacturing.

For the larger cross-section geometries shown, the process parameters chosen were suitable for the AFM method to improve the surface quality. For smaller cross-sections, however, these parameters were unsuitable, as illustrated in Fig. 11.

Figure 11 shows that after post-processing, the surface (centre) was significantly more undulated than in the as-built state (top). This can be attributed to the formation of cavitation-like spalling within the flow channels during post-processing, which, according to the responsible industrial partner, is a known phenomenon of the AFM process for small cross-sectional areas.

After adjustment of the carrier fluid and reduction of the extrusion pressure, a second post-processing step was then carried out, the negative imprint of which is shown at the bottom of Fig. 11. It can be seen that most of the previously formed grooves could be removed from the channel, although some local maxima remained.

5.2 Shape accuracy

The shape accuracy is defined as the deviation of the cross-sectional areas after manufacturing and post-processing compared to the dimensions of the original CAD models. To determine this shape accuracy, the CT scans were analysed before and after post-processing and their results were compared accordingly.

Exemplary for these investigations are the results of the diameters for the circular samples with 8 mm (large—L) and 2 mm (small—S) diameter shown in the following Fig. 12. The graphs with “SA” show the results of the solution-annealed samples and the graphs with “PH” those of the precipitation-hardened ones. The measurements before post-processing using AFM are shown in light and the measurements after are shown in dark.

The graphs show that all the specimens have only a slight deviation of about 50 μm from their nominal CAD geometry of 4 mm or 1 mm, which indicates good shape accuracy of the LPBF. Furthermore, a significantly higher increase in the radius of the post-processed specimens with a small cross-section can be seen, both in terms of absolute and

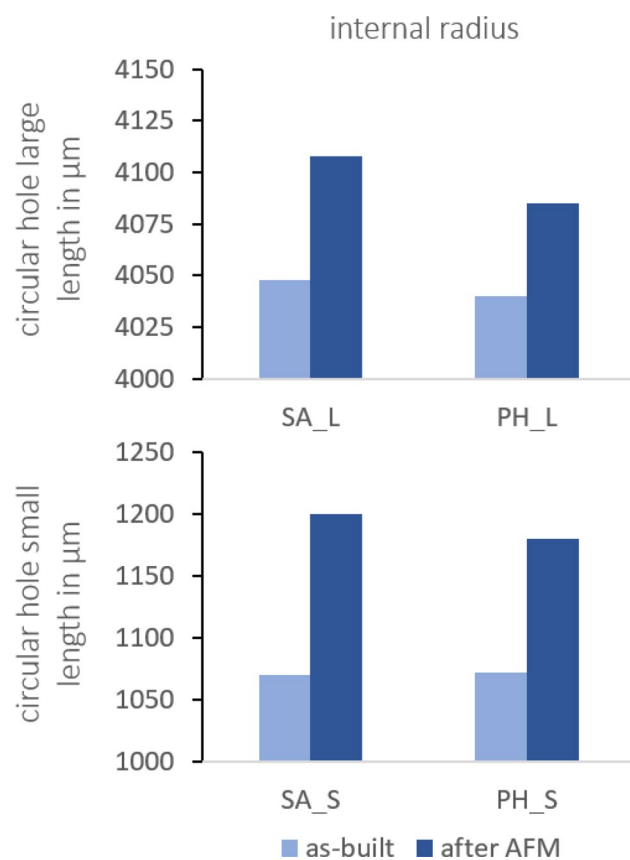


Fig. 12 Absolute change of the internal radius before and after post-processing; SA solution annealed and PH precipitation-hardened, nominal radii 4 mm (top) and 1 mm (bottom)

relative deviations. The samples with a diameter of 2 mm had an expansion of their internal radii of around 12.1% in the solution-annealed state and 10.1% in the precipitation-hardened state. The specimens with a diameter of 8 mm, in contrast, only had a relative increase in the internal radii of 1.5% (SA) and 1.1% (PH). This increased widening of the channel geometries with a 2 mm diameter is primarily due to the aforementioned second post-processing step after the previously mentioned cavitation-like conditions occurred in the channels.

Compared to the diagrams for the circular samples, the investigated rectangular geometries generally show similar results, whereby the relative deviations for small and large cross-sections are less pronounced. Again, a greater widening of the channels can be seen in samples that have only been solution annealed. For example, the elongation of the short side of 2 mm of the specimens with $8 \times 2 \text{ mm}^2$ cross-section for the solution-annealed condition was about 5%, while the elongation in the precipitation-hardened condition was only 1.5% (see Fig. 13). For the long side b with 8 mm nominal length, the elongation is smaller in both cases, with

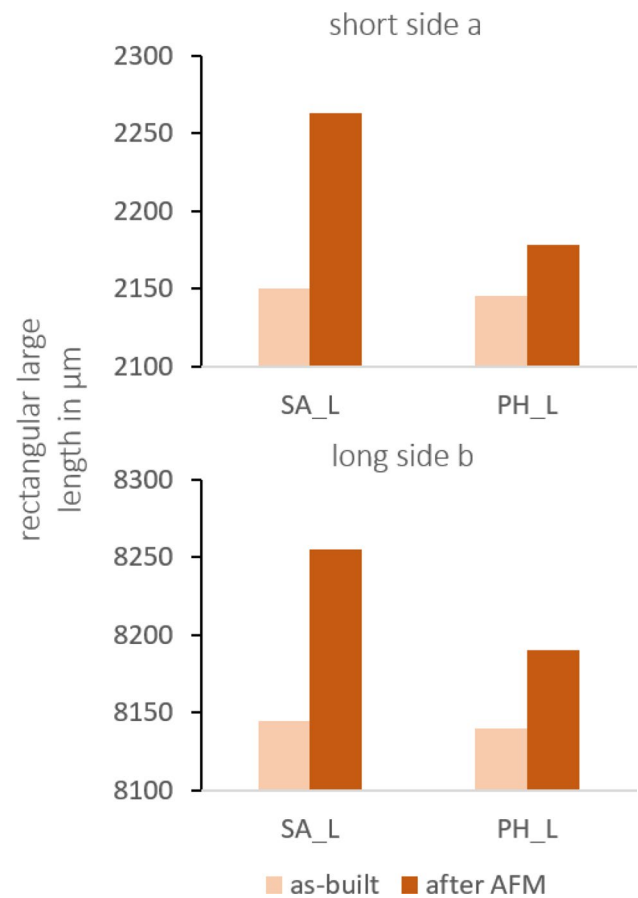


Fig. 13 Absolute change of the short side a and the long side b of a sample with a large rectangular cross-section ($8 \times 2 \text{ mm}^2$) before and after post-processing

about 1.3% in the solution annealed condition and 0.6% in the precipitation-hardened condition.

In terms of the shape accuracy in relation to the heat treatment, a smaller ablation rate can be observed for the hardened samples. Since a smaller deviation of the final geometries compared to their as-built state allows a better accuracy of the prediction of flow within the channels, it was decided for the following samples (as discussed in Sect. 3.1) to post-process all of them in the precipitation-hardened state.

6 Flow studies

In addition to profound investigations of the influence of AFM on surface roughness and shape accuracy, extensive investigations of the resulting improvement of flow through post-processed channels have been further carried out. The specimens investigated for this purpose are derived from the overview of channel geometries in Sect. 3.1. Of the 34 possible variants presented there, a total of 23 specimens were successfully manufactured using LPBF. In the case of the other 11 variants, process interruptions occurred during manufacturing, preventing them from being available in time for the flow tests.

To investigate the improvement in flowability as a result of post-processing with AFM, all specimens were measured both before and after post-processing. An existing test facility at the ILR [24, 25] was used to measure the mass flow of the fluid, the inlet and outlet pressure across the samples, and the fluid temperature. To reduce the experimental effort and considering the planned water-cooled aerospike demonstrator (see Sect. 7), all flow tests were performed with tap water.

6.1 Post-processing approach

For post-processing using AFM, the findings of the preliminary study (see Sect. 5) were taken into account for the specimens of the flow investigations. On the one hand, this led to the use of abrasive media with a comparatively lower viscosity and smaller grinding particles. This approach aimed to improve the flow during post-processing and to reduce the occurrence of cavitation-like effects (see Fig. 11). As in the previous study presented in Sect. 5 fluids from ExtrudeHone and 4MI were used as abrasive media, the former primarily for straight specimens and the latter for angled specimens with 45° and 90°. While the exact composition of 4MI media is subject to secrecy, the ExtrudeHone medium used is composed of a carrier fluid of polyborosiloxane polymers and abrasive silicon carbide particles. The extrusion pressure was slightly increased compared to the preliminary study, resulting in 35–45 bar for channels with

a cross-section larger than 4 mm² and 43–56 bar for smaller cross-sections. The temperatures of the abrasive media during post-processing were in the range of about 21–30 °C and, therefore, slightly lower than during post-processing of the specimens in Sect. 5. As in the preliminary study, the post-processing was performed without counterpressure and the flow direction was reversed about halfway through the processing time. The processing time was subject to large variations depending on the post-processed cross-sections and the initial roughness, with durations ranging from 120 to 1000 min per specimen. The same applies to the amount of abrasive medium used with values ranging from 200 to 1000 in.³, whereby two specimens with a diameter of 8 mm in fact required over 4000 in.³. Since it was observed at the beginning of the post-processing that some samples only allowed a low flow during AFM, it was decided to pre-process all samples using microblasting. Hereby, sintered powder residues were removed from the channels as well as any excessive peaks in surface roughness, which enabled a better initial flow rate during AFM. For microblasting, the fine blasting unit F-S40 of Harnisch + Rieth was used with the stainless-steel blasting media Chronital.

6.2 Experimental results

Of the 23 specimens provided by Fraunhofer IWS, a comparison of the flowability before and after processing by AFM was performed for a total of 16 specimens. All investigated combinations of cross-section and channel shapes are shown in Table 3 together with the percentage improvement

Table 3 Overview of the percentage change in the kV value for all investigated flow samples; channel shapes corresponding to Fig. 4

Cross-section	Channel shape	Change of kV value in %
Circular Ø 2 mm	Straight	+15
Circular Ø 4 mm	(d)	+16
Circular Ø 8 mm	Straight	+21
Circular Ø 8 mm	(a) 2×45°	+31
Circular Ø 8 mm	(a) 2×90°	+30
Circular Ø 8 mm	(b)	+25
Circular Ø 8 mm	(d)	−1
Rectangular 4×1 mm ²	Straight	+41
Rectangular 4×1 mm ²	(a) 2×90°	+154
Rectangular 4×1 mm ²	(c) Ø 4 mm	+3
Rectangular 4×2 mm ²	(a) 2×45°	+83
Rectangular 4×2 mm ²	(b)	+120
Rectangular 4×2 mm ²	(d)	+43
Rectangular 8×1 mm ²	(a) 2×45°	+28
Rectangular 8×2 mm ²	(a) 2×90°	+27
Rectangular 8×2 mm ²	(c) Ø 8 mm	+1

of the kV values. The missing comparison of the other seven specimens was mostly due to non-determinable flow rates before AFM, caused by sintered particles within the channels, which prevented a comparison with kV values after AFM. The blockage of these specimens by sintered particles was confirmed by later CT scans.

As shown in Table 3, an increase in flow rate, represented by the kV value, was generally achieved using post-processing via AFM, with the exception of one specimen. The measured mass flow rates on which the calculation of the kV values was based were in the range of about 50–200 g/s. As can be seen, the percentage change is subject to substantial dispersion. In general, however, it could be observed that for a large part of the specimens with a small percentage increase, a low pressure drop at comparatively high mass flows could already be determined before AFM, which also applies to the specimen with reduction of the kV value. Thus, for these specimens, the roughness reduction by AFM had only a small effect on improving the flow rate. For specimens with a very high percent improvement in kV value, CT scans prior to AFM mostly showed a greater percentage of sintered particles, suggesting that these sinterings were reduced by the abrasive medium. However, verification of this assumption is still pending, as the evaluation of CT scans after AFM have not yet been fully evaluated. A specific correlation between cross-section, channel shape and increase in kV value could not be determined so far during the investigation of the 16 specimens, partly due to the missing results in relation to the initial specimen scope.

The correlation of the determined flow parameters to the actual surface roughness of the samples before and after AFM remains to be determined. An initial approach was to evaluate the roughness values based on CT data. However, due to overlapping of the noise of the CT images with the roughness values to be determined, this method was found to be not sufficiently accurate. While silicone imprints of surface roughness were also made, as in the preliminary study, they are not entirely suitable for correlation to flow parameters. This is due to the fact that the imprints could only be obtained in straight sections of the specimens and, therefore, do not reflect the roughness values in curved sections, such as those found in specimens with 45° or 90° change of flow direction. The now pursued approach is the direct tactile measurement of the cut open specimens after AFM as well as of identical specimens without post-processing.

7 Aerospike-engine design

To apply the findings of the previously described investigations beyond the test specimens, the ILR is pursuing the development of another aerospike demonstrator in parallel. This engine will be based on the 2019 demonstrator

presented in Sect. 1 and will retain its intended performance parameters. This will enable the comparability of both engine demonstrators with regard to the adjustments to the design and the findings from the manufacturing studies.

An important change compared to the previous design is the subdivision of the engine into three instead of two individual components, enabled by the separation of the injector plate and the spike. This additional subdivision will improve accessibility for post-processing steps and allow better positioning and alignment of the individual parts during manufacturing. In addition, these individual components will be connected using a flanged joint as opposed to a welded joint, which was used in the previous engine. This will allow individual components to be exchanged, making it possible to investigate injectors that have been post-processed by different means.

Figure 14 shows a section through the CAD model of the revised aerospike engine. The depiction shows the cooling channels within the combustion chamber and the spike walls, as well as the injector feed lines for the dual-impingement injector. Figure 15 shows the combustion chamber after successful manufacturing at the Fraunhofer IWS using LPBF. Currently, all three parts of the engine have been manufactured and heat treated. Still pending is the mechanical post-processing of the individual parts and the completion of the assembly.

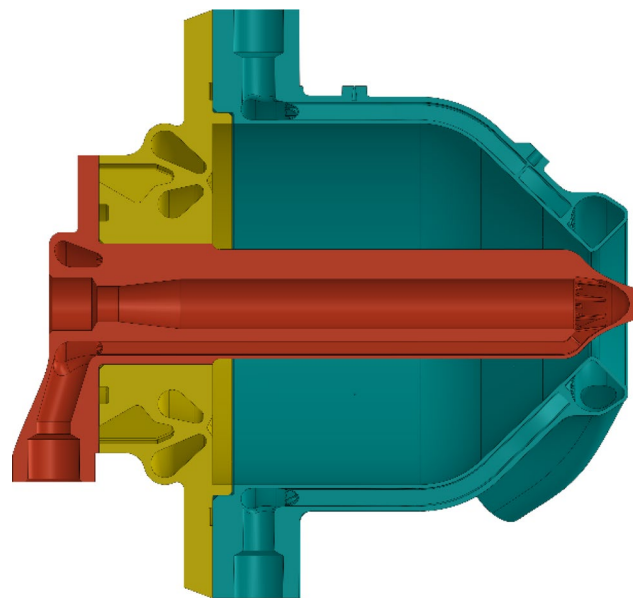


Fig. 14 Current aerospike design consisting of combustion chamber (cyan), injector plate (yellow) and spike (red)



Fig. 15 Combustion chamber of the newly designed aerospike engine after manufacturing via LPBF

8 Summary

In this article, the influence of additive manufacturing using laser powder bed fusion on the surface quality of flow channels was presented. It was demonstrated that, in a direct comparison, a layer thickness of 30 μm is preferable to 60 μm , as the resulting structures had a smaller number of material inclusions and, as a result, a higher tensile strength. In combination with the predicted improved thermal conductivity of the 30 μm layer, it is preferable for the manufacturing of cooling channels. With regard to overhang angles, the investigations confirmed previous observations that the surface roughness increases significantly as the overhang angle decreases relative to the construction platform.

In addition, the post-processing of first test specimens by means of abrasive flow grinding and the findings obtained were described. It became apparent that the cross-sectional area has a direct impact on the post-processing results, where cavitation-like effects can occur for smaller cross-sections during post-processing. The relationship between heat treatment and finishing was also investigated, with initial studies showing that precipitation-hardened samples show similar surface roughness values with higher shape accuracy after flow grinding compared to only solution-annealed samples.

Furthermore, flow tests were carried out with a number of different test specimens, which differed in cross-sectional area and channel shape. By measuring the mass flow and pressure drop across the specimens before and after post-processing with AFM, the influence on the flow rate was considered. Current results show that in general an improvement of the flow rate can be achieved by post-processing with AFM and sintered particles can be effectively removed from the channels. An exact correlation between channel cross-section and post-processing result could not be derived

at this stage and requires further investigation as well as a comparison of the roughness values of the flow samples.

Some of the findings have already been incorporated into a revised aerospike demonstrator, which has already been successfully manufactured via additive manufacturing. Following the currently pending post-processing, an experimental investigation of this engine is planned in a hot fire test campaign at the beginning of 2023.

Acknowledgements We would like to thank the German Federal Ministry of Education and Research for funding the project CFDMikroSAT (Förderkennzeichen 03ZZ0232D) within the AGENT3D program as well as our industrial partner AM Metals for performing the AFM post-processing. Here we would also like to thank our colleagues at the Institute of Aerospace Engineering, especially Jan Sieder-Katzmann and Tim Dorau, for their valuable contribution within the project. In addition, the authors gratefully acknowledge the various students at the Fraunhofer Institute for Material and Beam Technology and the Technische Universität Dresden for their continuous support, contributing substantially to the progress of the presented investigations.

Funding Open Access funding enabled and organized by Projekt DEAL.

Declarations

Conflict of interest There are no potential conflicts of interest for the authors to disclose. There are no financial interests to record, and all co-authors have seen and agreed with the contents of the work. We certify that the submission is unique and that it is not currently under consideration by another publisher.

Open Access This article is licensed under a Creative Commons Attribution 4.0 International License, which permits use, sharing, adaptation, distribution and reproduction in any medium or format, as long as you give appropriate credit to the original author(s) and the source, provide a link to the Creative Commons licence, and indicate if changes were made. The images or other third party material in this article are included in the article's Creative Commons licence, unless indicated otherwise in a credit line to the material. If material is not included in the article's Creative Commons licence and your intended use is not permitted by statutory regulation or exceeds the permitted use, you will need to obtain permission directly from the copyright holder. To view a copy of this licence, visit <http://creativecommons.org/licenses/by/4.0/>.

References

1. Sanchez, S., Smith, P., Xu, Z., Gaspard, G., Hyde, C., Wits, W., Ashcroft, I., Chen, H., Clare, A.: Powder bed fusion of nickel-based superalloys: a review. *Int. J. Mach. Tools Manuf.* **165**, 3–5 (2021)
2. Minet, K., Saharan, A., Loesser, A., Raitanen, N.: 8—Superalloys, powders, process monitoring in additive manufacturing. In: *Additive manufacturing for the aerospace industry*, pp 163–185 (2019)
3. Witt, G., Wegner, A., Sehr, J.T.: Neue Entwicklungen in der Additiven Fertigung. In: *Beiträge aus der wissenschaftlichen Tagung der Rapid Tech 2015* (2015)
4. Gradl, P., Greene, S.E., Protz, C., Bullard, B., Buzzelt, J., Garcia, C., Wood, J., Cooper, K., Hulka, J., Osborne, R.: Additive manufacturing of liquid rocket engine combustion devices: a summary

- of process developments and hot-fire testing results. In: 54th AIAA/SAE/ASEE 2018.
5. Bach, C.: Systemanalyse und Prototypenentwicklung einer durch Fluidinjektion induzierten Schubvektorsteuerung für Aerospike-Triebwerke, Dresden, Germany (2019)
 6. Defusco, A., Craddock, C.: Affordable access to low earth orbit. *DSIAC J.* **4**, 4–12 (2017)
 7. Besnard, E., Garvey, J.: Aerospike engines for nanosat and small launch vehicles (NLV/SLV). In: Space 2004 Conference and Exhibit, San Diego, California (2004)
 8. Buchholz, M., Gloder, A., Gruber, S., Marquardt, A., Meier, L., Müller, M., Propst, M., Riede, M., Selbmann, A., Sieder-Katzmann, J., Tajmar, M., Bach, C.: Developing a roadmap for the post-processing of additively manufactured aerospike engines. In: 71th International Astronautical Congress (IAC) (2020)
 9. Stimpson, C.K., Snyder, J.C., Thole, K.A., Mongillo, D.: Roughness effects on flow and heat transfer for additively manufactured channels. *ASME. J. Turbomach.* **138**(5), 051008 (2016). <https://doi.org/10.1115/1.4032167>
 10. Gibson, I.G., Rosen, D., Stucker, B.: Additive Manufacturing Technologies: 3D Printing, Rapid Prototyping and Direct Digital Manufacturing. Springer, Berlin (2015)
 11. Gebhardt, A., Kessler, J., Thurn, L.: 3D-Drucken: Grundlagen und Anwendungen des Additive Manufacturing (AM), Hanser (2016)
 12. Brandl, E., Heckenberger, U., Holzinger, V., Buchbinder, D.: Additive manufactured AlSi10Mg samples using selective laser melting (SLM): Microstructure, high cycle fatigue and fracture behavior. *Mater. Des.* **34**, 159–169 (2012)
 13. Prabhu, S., Mallikarjun, V., Kumar, S., Shivaram, P.R., Sb, N.K., Gupta, N., Sekar, V.: Comparative study on the machining of Ti-6Al-4V titanium alloy and Inconel 718 super alloy. In: IND-BRAZIL Bilateral International Conference on Advanced Materials and Manufacturing (ICAMM 2015), Tirunelveli, India (2015)
 14. Smith, R.J., Lews, G.J., Yates, D.H.: Development and application of nickel alloys in aerospace engineering. *Aircr. Eng. Aerosp. Technol.* **73**(2), 138–146 (2001)
 15. Peters, M., Kumpfert, J., Ward, C.H., Leyens, C.: Titanium alloys for aerospace applications. *Adv. Eng. Mater.* **5**(6), 419–427 (2003)
 16. Altaf, M., Dwivedi, S.P., Kanwar, R.S., Siddiqui, I.A., Sagar, P., Amad, S.: Machining characteristics of titanium Ti-6Al-4V, Inconel 718 and Tool Steel—a critical review. In: International Conference on Computational and Experimental Methods in Mechanical Engineering (ICCMME), India (2019)
 17. VDM Metals: Data sheet Inconel 718 (2019)
 18. DEW Stahl: Data sheet 1.2344 (2019)
 19. Jain, N., Jain, V.: Modeling of material removal in mechanical type advanced machining processes: a state-of-the-art review. *Int. J. Mach. Tools Manuf.* **41**, 1573–1635 (2001)
 20. Uhlmann, E., Schmiedel, C., Wendler, J.: CFD simulation of the abrasive flow machining process. *Procedia CIRP.* **31**, 209–214 (2015)
 21. Ramkumar, J., Jain, V., Sankar, M.: Abrasive flow machining (AFM): an overview (2011)
 22. Uhlmann, E., Wendler, J.: Development of a material model for visco-elastic abrasive medium in abrasive flow machining. *Procedia CIRP.* **8**, 351–356 (2013)
 23. Khan, H.M., Karabulut, Y., Kitay, O., Kaynak, Y., Jawahir, I.S.: Influence of the post-processing operations on surface integrity of metal components produced by laser powder bed fusion additive manufacturing: a review. *Mach. Sci. Technol.* **25**(1), 118–176 (2020)
 24. Bach, C., Sieder, J., Przybliski, O., Tajmar, M.: SMART rockets: development of a 500 N LOX/ethanol-sounding rocket for the DLR STERN programme. In: 62. Deutscher Luft- und Raumfahrt-kongress (DLRK), Stuttgart, Germany (2013)
 25. Sieder, J., Bach, C., Przybliski, O., Tajmar, M.: SMART rockets: a contribution to the DLR STERN programme by Dresden University of Technology. In: 5th European conference for aeronautics and space sciences (EUCASS), Munich, Germany (2013)

Publisher's Note Springer Nature remains neutral with regard to jurisdictional claims in published maps and institutional affiliations.